Microstructure, Mechanical Properties, and Crack Propagation Behavior in High-Nb TiAl Alloys by Directional Solidification

QI WANG, RUIRUN CHEN, XUE GONG, JINGJIE GUO, YANQING SU, HONGSHENG DING, and HENGZHI FU

Titanium aluminide (Ti-47Al-6Nb-0.1C) alloys were prepared using a cold crucible directional solidification technique with an input power range of 35 to 55 kW under a withdrawing velocity of 0.4 mm/min. The macro/microstructure was characterized, and the mechanical properties were evaluated. The results show that the directional solidification (DS) ingots exhibit β-solidification characteristics at an input power range of 35 to 55 kW, and a well-developed DS microstructure was acquired at an input power range of 40 and 45 kW. With the increasing input power, the lamellar spacing decreases, resulting in the increasing tendency in the average room-temperature yield strength. The steady-state creep rate strongly depends on the lamellar spacing, and the creep life depends on the DS microstructure. The well-developed DS alloy can significantly improve the creep properties but has little influence on the room-temperature tensile properties. Moreover, after testing the fracture toughness, the crack propagation showed interlamellar cracks, translamellar cracks, and intercolony boundary cracks that primarily propagated along the colony boundary after creep testing.

I. INTRODUCTION

TITANIUM aluminide alloys based on the intermetallic gamma phase are widely considered to be a replacement for Ni-based superalloys above 600 °C due to their low density and high specific strength.[1–3] Compared with conventional TiAl alloys, high Nb-containing TiAl alloys exhibit superior high-temperature strength and oxidation resistance.[4,5] However, Nb as a β-stabilizer usually induces the formation of the β(B2) phase in the matrix at room temperature, which is harmful to the room-temperature tensile properties and high-temperature creep properties of the material.[5,6] In addition, the B2 phase in the matrix can result in stress concentration, which induces the formation of cracks in the bulky B2 phase that propagate along its boundaries.[7,8] Therefore, it is essential to restrict the formation of the B2 phase in the as-cast high Nb TiAl alloy. Chen et al.[9] reported that three $\alpha_2 + \gamma + $ B2 phases can form in lamellar structures and that two B2 $+ \gamma$ phases

can form at the colony boundary during solidification when the β-stabilizing elemental content in the local segregation region exceeds a threshold value. According to the ternary phase diagrams of Ti-Al-Nb,[9,10] the region of the three $\alpha_2 + \gamma + $ B2 phases can form in the low-Al region. This finding indicates that both high Nb and high Al contents in the TiAl alloy will restrict the formation of the B2 phase. In addition, the high Al content can improve the room-temperature elongation in fully lamellar TiAl alloys.[10] Therefore, the combination of high Al and high Nb contents in the as-cast TiAl alloys restricts the formation of the B2 phase and maintains a balance between the room-temperature tensile properties and the high-temperature creep properties.

The microstructure of TiAl alloys has a significant influence on the room-temperature tensile properties and high-temperature creep properties of the material, and the microstructure strongly depends on the solidification technique. Yamaguchi and Inui have reported the directional solidification (DS) technique with TiAl alloys in detail.[11–13] A homogeneous and stable microstructure showing significant anisotropy in the mechanical properties can be obtained using the DS technique.[14] However, the use of ceramic crucibles usually leads to the formation of contamination due to ceramic inclusion in the molten TiAl alloys during the DS process due to the high melting and high activity of

QI WANG, RUIRUN CHEN, XUE GONG, JINGJIE GUO, YANQING SU, HONGSHENG DING, and HENGZHI FU are with the School of Materials Science and Engineering, Harbin Institute of Technology, Harbin 150001, China. Contact e-mail: ruirunchen@hit.edu.cn

TiAl alloys. This effect significantly reduces the room-temperature tensile properties and high-temperature creep properties of the material.[15,16] The electromagnetic cold crucible directional solidification (CCDS) technique can prevent the formation of contaminants and can be used to prepare industrial sizes, offering defect-free DS microstructures.[17,18] Moreover, the grain size can be controlled using the input power during the CCDS process, thus providing a method to study the effect of grain size on the creep behavior. Previous studies have reported that the high-temperature creep properties decreased with a decrease in grain size.[19–21] However, these studies were mostly conducted through heat treatment or with the addition of refining elements. The α_2/γ lamellae and colony boundaries significantly changed after the heat treatment. The addition of refining elements, such as B and Y elements, can induce the formation of a precipitated phase in the matrix, which provides increasing opportunity for cavity nucleation at colony boundaries.

In the current study, the Ti-47Al-6Nb-0.1C alloy was prepared using the CCDS technique with an input power range of 35 to 55 kW. The influence of the input power on the macro/microstructure, room-temperature tensile properties, fracture toughness, and creep behavior was systematically investigated. Attention is given to the crack propagation behavior in creep and fracture-toughness specimens.

II. EXPERIMENTAL PROCEDURES

A. Materials and CCDS Ingot Preparation

The Ti-47Al-6Nb-0.1C alloy with an actual composition of Ti-47.36Al-5.76Nb-0.1C was supplied in the form of an as-cast cylindrical ingot that was produced by induction skull melting (ISM) combined with the vacuum consumable melting (VAR) techniques. The VAR process was conducted under an argon atmosphere. The samples for directional solidification with a 280 mm length and 24 mm diameter were cut along the axial direction of the ingot. The DS experiments were performed based on a multifunctional electromagnetic solidification apparatus equipped with a square, cold crucible (36 mm × 36 mm). The experimental details have been previously described.[18] The CCDS bars were solidified under a withdrawing velocity of 0.4 mm/min for 150 minutes and an input power range of 35 to 55 kW.

B. Room-Temperature Tensile Tests and High-Temperature Creep Tests

The room-temperature tensile test was carried out on a 5569 Instron testing machine under a tensile speed of 0.5 mm/min. The gauge length section of the specimens was 20 mm × 6 mm × 2 mm. The elongation was measured by an extensometer. At least five qualified samples of each CCDS ingot were tested. Based on these tests, the statistical results of yield stress and elongation for each CCDS ingot were obtained. The ingots were cut into creep specimens along the axial direction with a cross section of 4.5 mm × 2.5 mm and a gauge length of

20 mm. The creep tests were performed in air under a constant load in a GWT504-model creep testing machine. The room-temperature tensile testing samples and creep samples were cut from the DS region along the axial direction. The displacement was recorded by two linear variable differential transducers, and the creep temperature was measured by a thermoelectric couple device. The size (mm) of the specimen for the room-temperature tensile tests is shown in Figure 1(a), and that for the creep tests is shown in Figure 1(b).

C. Fracture Toughness

The single edge notched bend (SENB) specimens were used to test the fracture toughness of the alloys. The fracture toughness specimens were cut from the DS region along the pulling direction. At least five qualified samples of each CCDS ingot were tested. Based on these tests, the statistical results of the K_{IC} value for each CCDS ingot were obtained. The detailed dimensions of the specimens are shown in Figure 1(c). An electrode discharge machine was used to create 2.0-mm-deep slit notches in the specimens. The Instron-5500 testing machine was used to conduct the fracture toughness testing with a crosshead displacement rate of 3 μm/s^{-1}. The fracture load can be observed from the load–displacement curves, and the K_{IC} values can be expressed as

$$K_{IC} = (P \cdot S/B \cdot W^{3/2}) \cdot f(a/w)$$
$$f(a/w) = 3(a/w)^{1/2}$$
$$\cdot \frac{1.99 - (a/w)(1 - a/w)[2.15 - 3.93(a/w) + 2.7(a/w)^2]}{2(1 + 2a/w)(1 - a/w)^{3/2}}$$

where P corresponds to the load determined at the 95 pct slope of the linear elastic part of the load–displacement curves; W corresponds to the width of the specimen; B corresponds to the thickness of the specimen; a corresponds to precrack length, including the slit notch; and S corresponds to the span of the load ($S = 4W$).

D. Microstructure Investigation

The CCDS ingots were cut into two isometric halves longitudinally. The macrostructure of the CCDS ingots was recorded with a Nikon D800 digital single lens reflex camera. The scanning electron microscopy (SEM) specimens were polished and etched in modified Kroll's reagent composed of 28 vol pct HF, 2 vol pct HNO$_3$, and 70 vol pct H$_2$O. The microstructure was observed with Quanta 200FEG SEM in backscattered electron mode (BSE). Transmission electron microscopy (TEM) specimens were first cut using wire electrodes to approximately 400 μm and later ground to approximately 70 μm, followed by twinjet electropolishing in a solution of 60 pct methanol, 35 pct butyl alcohol, and 5 pct perchloric acid at 15 V and – 35 °C. A Tecnai G2 F30 TEM was used to measure the lamellar spacing under the edge-on position, which was acquired from the line intercept method. The lamellar spacing of each ingot was measured from ten TEM images and calculated ten times. Based on these measurements, the statistical
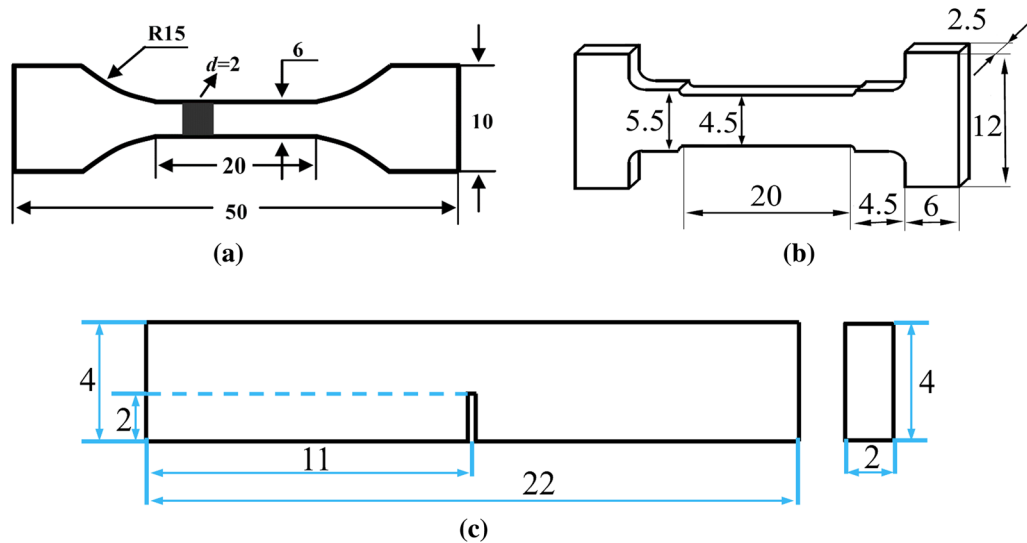
Fig. 1—Size (mm) of the specimens for (*a*) room-temperature tensile tests, (*b*) creep tests, and (*c*) fracture toughness tests.
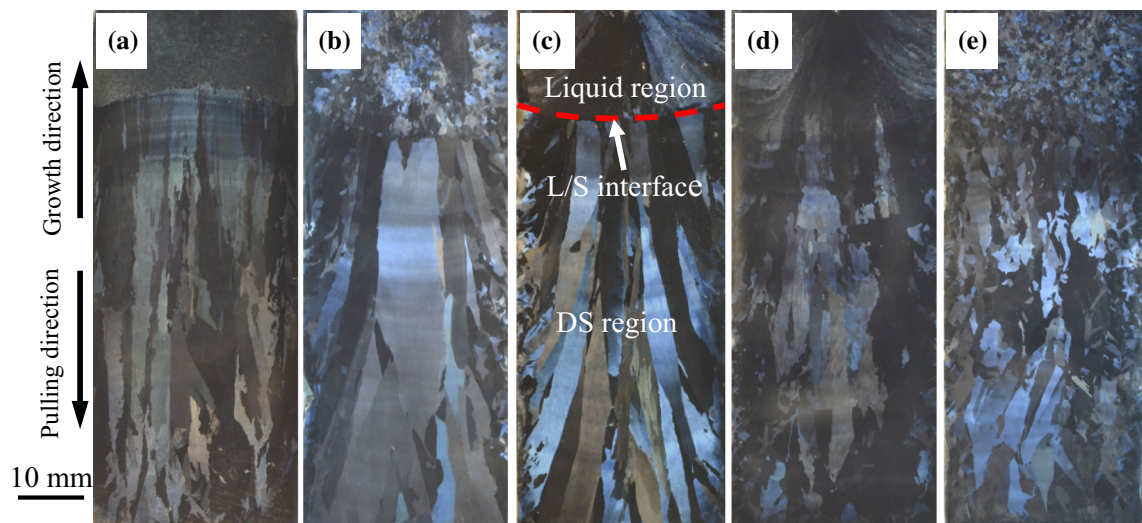

Fig. 2—Macrostructures of the CCDS ingots under a growth rate of 0.4 mm/min and different power levels: (*a*) 35 kW, (*b*) 40 kW, (*c*) 45 kW, (*d*) 50 kW, and (*e*) 55 kW.

results of the lamellar spacing were obtained. The lamellar orientations (lamellar angle between the loading axis and the lamellar boundaries) of each CCDS ingot were investigated using an optical microscope (OM), and the lamellar orientations were measured at the well-developed DS region in each CCDS ingot. Based on these observations, the statistical results of the lamellar orientations were obtained.

III. RESULTS AND DISCUSSION

A. *Macrostructure*

Figure 2 shows the macrostructure of the CCDS ingots that were prepared under a growth rate of 0.4 mm/min

and an input power of 35 to 55 kW. As seen in Figures 2(b) and (c), the well-developed DS ingots are obtained when the input power is 40 or 45 kW. Meanwhile, the columnar grains are continuous along the growth direction. The discontinuous columnar grains observed in Figures 2(a), (d), and (e) correspond to power levels of 35, 50, and 55 kW, respectively. The final solidification region (liquid region) and the DS region are divided by the liquid/solid (L/S) interface, as shown in Figure 2(c). In the CCDS process, the temperature gradient and electromagnetic stirring increase with the increasing input power.[22] Therefore, both the temperature gradient and electromagnetic stirring can affect the macrostructure and microstructure in the CCDS ingots. The samples are analyzed through a combination of these

factors with the dendrite morphologies at the front of the S/L interfaces as described herebelow.

B. *Microstructure*

After a sudden electricity failure, the liquid region in front of the S/L interface was rapidly solidified, and the initial solidification morphology of the CCDS could be observed. Figure 3 shows the dendrite morphologies near the front of the S/L interfaces corresponding to Figures 2 (a) through (e). The typical β-solidification characteristics are observed in Figures 3(b) through (e) (prepared at 40 to 55 kW) since the second dendritic arms are perpendicular to the primary dendritic arms. Several equiaxed grains are found in the front of the S/L interfaces in Figure 3(a) (prepared at 35 kW). When the input power is in the range of 40 to 55 kW, well-developed dendrite morphologies are observed. However, when the power increases to 55 kW, the obvious existence of columnar grains and equiaxed grains can be found at the front of the S/L interfaces, as shown in Figure 3(e).

During the CCDS process, as the input power increases, the dendrite morphologies at the front of the L/S interface change from equiaxed grains to columnar grains (from 35 to 40 kW) and later change from columnar grains to equiaxed grains. This result can be interpreted from Eqs. [1] through [4] [23,24]:

$$\Delta T_n = T_L(C_0) - T_n \qquad [1]$$

where $T_L(C_0)$ corresponds to the liquid line temperature of the C_0 alloy, T_n corresponds to the nucleation temperature of the equiaxed grain, and ΔT_n corresponds to the supercooling of the equiaxed nucleation.

$$\Delta T_t = T_L(C_0) - T_t \qquad [2]$$

In this equation, T_t corresponds to the temperature of the columnar dendrite tip, and ΔT_t corresponds to the supercooling of the columnar nucleation. The columnar to equiaxed transition (CET) of the solidification microstructure emerges as the temperature gradient (G) meets the following criteria (ideal conditions):

$$G < 0.617 N^{1/3} \cdot \Delta T_t \cdot \left(1 - \left(\frac{\Delta T_n}{\Delta T_t}\right)^3\right) \qquad [3]$$

In this inequality, N corresponds to the nucleation rate. In Eq. [3], the ΔT_t and growth rate (V) can be expressed as

$$\Delta T_t \propto V^{1/2} \qquad [4]$$

According to Eqs. [1] through [4], the CET depends on the temperature gradient (G), nucleation rate (N) and growth rate (V). At low-temperature gradients (G), high growth rates (V) or high nucleation rates (N), the CET is inclined to occur during the CCDS process. In the current study, several equiaxed grains are found at the front of the S/L interfaces due to the low-temperature gradient (G) at a power of 35 kW. The well-developed DS ingots were acquired at power levels of 40 to 45 kW due to the appropriate temperature gradient (G), growth rate (V) and nucleation rate (N). Several well-developed columnar grains and dissociative equiaxed grains exist in the solid + liquid phase region at the front of the S/L interfaces at a power of 55 kW since the high-temperature gradient (G) and high electromagnetic stirring improve the nucleation rate (N), thus promoting CET. Moreover, the dendrite arm may fuse or break off at high electromagnetic stirring rates,[25,26] thus promoting the formation of equiaxed grains and destroying the DS
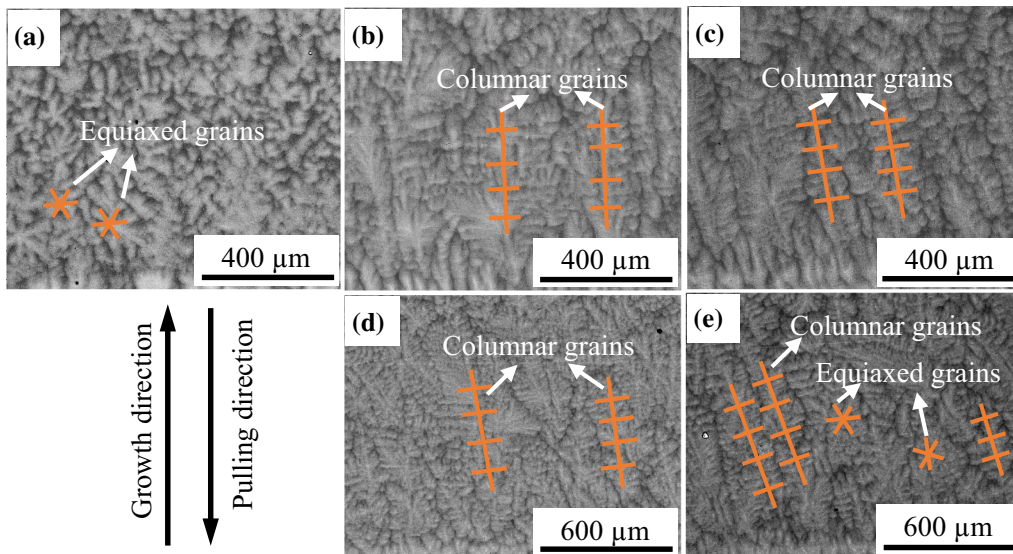

Fig. 3—Microstructure at the front of the L/S interface at different power levels: (*a*) 35 kW, (*b*) 40 kW, (*c*) 45 kW, (*d*) 50 kW, and (*e*) 55 kW.

macrostructure. According to the discussions above, Figure 4 shows a schematic of the influence of the power on the solidification path and macro/microstructure during the CCDS process at (a) 35 kW, (b) 40 to 45 kW and (c) 55 kW. It is clear that the appropriate input power is important for well-developed DS macro/microstructures.

Figure 5 shows the microstructure of the original as-cast and CCDS Ti-47Al-6Nb-0.1C alloys. The Nb segregation can be found in the as-cast microstructure, as marked and shown in Figure 5(a). Figures 5(b) and (c) show the microstructure under the input power of 45 kW and 55 kW, corresponding to Figures 2(b) and (d). Nb segregation can also be observed in the matrix, but
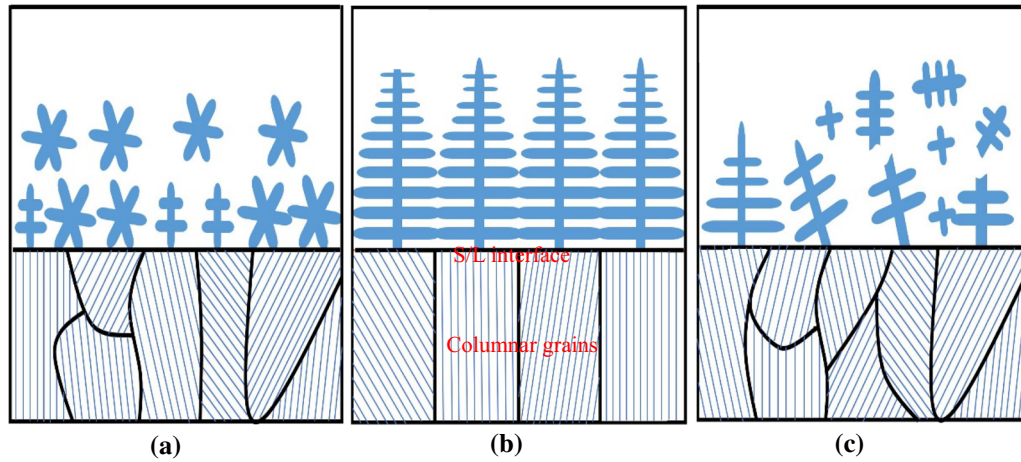

Fig. 4—Schematic illustration of the influence of the power on the solidification path and macro/microstructure: (a) 35 kW, (b) 40 to 45 kW, and (c) 55 kW.
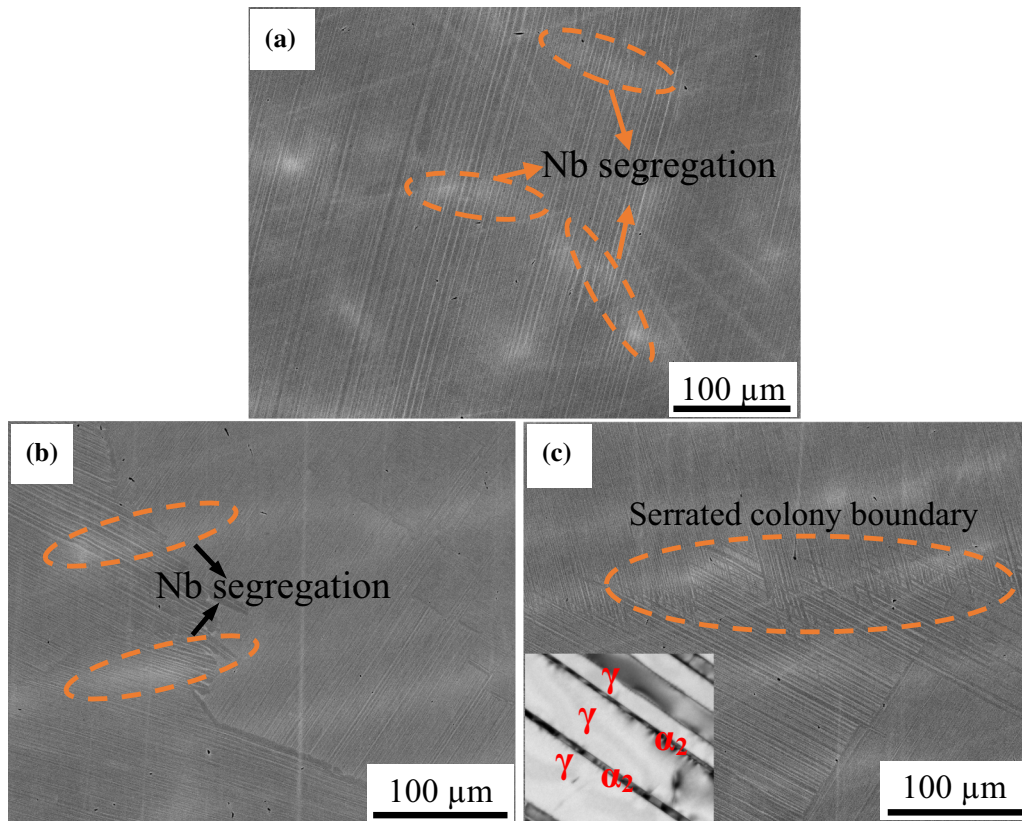

Fig. 5—SEM-BSE microstructure of the as-cast and CCDS ingots: (a) as-cast and (b) and (c) CCDS prepared under 45 and 55 kW, respectively.

Nb segregation in the CCDS alloys seems to be lower than that in the as-cast alloy. The molten pool can be thoroughly mixed under electromagnetic forces during the CCDS process, which reduces the inhomogeneity of the solute distribution. However, Nb diffuses slowly in the TiAl alloy due to its low diffusion coefficient.[9,10] The peritectic reaction promotes solute Nb to be distributed in the core of the dendrites;[4,5] thus, Nb segregation can be found in the matrix of the CCDS billets. Moreover, since there is a relatively sufficient diffusion resulting from the low solidification rate and the high Al content, there is no obvious presence of B2 phase in the matrix. The serrated colony boundary can be found in the matrix, as marked in Figure 5(c), and the TEM lamellar microstructure is shown in the inset of Figure 5(c). This alloy exhibits a fully lamellar microstructure.

C. Effect of Input Power on Grain Size, Lamellar Orientation, and Lamellar Spacing

In the fully lamellar TiAl alloy, the mechanical properties strongly depend on the microstructure characteristics. Table I lists the grain size as well as the statistical measurement results based on the room-temperature tensile tests, fracture toughness tests, lamellar spacing, and grain size measurements in each CCDS ingot in a power range of 35 to 55 kW. The well-developed DS ingots have continuous columnar grains along the growth direction. The effect of the power on the grain size is shown in Figure 6(a). Although there are more regions of equiaxed grains at an input power of 35 kW than those at an input power of 55 kW, the grain size at 55 kW is considerably smaller than that at 35 kW. This result indicates that high electromagnetic stirring rates can refine the grain size in the CCDS ingots.

The statistical measurement results of the lamellar orientations (lamellar angle ø between the loading axis and the lamellar boundaries) are shown in Figure 6(b). The lamellar orientations of the CCDS specimens in the power range of 35 to 55 kW are similar, and the lamellar angles ø in the range of 0 to 30 deg account for the majority of occurrences. The fully lamellar TiAl alloys possess better room-temperature tensile properties when the lamellar angles ø are in the range of 0 to 30 deg.[27] The lamellar spacing has a profound effect on the mechanical properties in the fully lamellar TiAl alloys. The fine lamellar spacing can improve the room-temperature tensile properties and high-temperature creep properties.[6,28] Figure 6(c) exhibits the statistical measurement results, revealing that the lamellar spacing decreases with higher power levels in the range of 35 to 55 kW for CCDS alloys.

D. The Room-Temperature Tensile Properties and High-Temperature Creep Properties

Figure 7 shows the room-temperature tensile properties of CCDS alloys in the power range of 35 to 55 kW corresponding to the values in Table I. The average room-temperature yield strength shows a tendency to increase with the increasing input power. The increase in the yield strength results from the decreasing lamellar spacing since the finer lamellar spacing of TiAl alloys can improve the room-temperature tensile properties. The grain size significantly decreases at a power of 50 and 55 kW. However, this change does not have an obvious influence on the room-temperature tensile properties. In the power range of 40 to 55 kW, this alloy exhibits relatively high average room-temperature

Table I. Grain Size, Lamellar Spacing, Yield Stress, Elongation, and Fracture Toughness at a Power Range of 35 to 55 kW

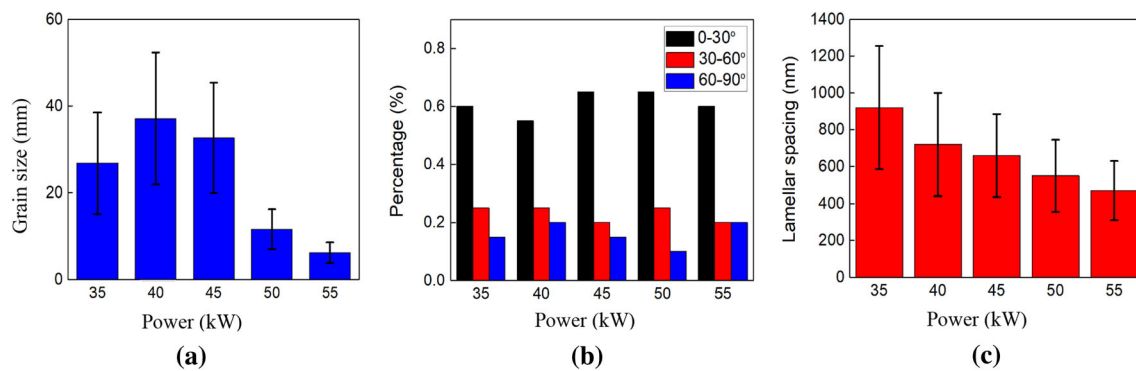| Power (kw)	35	40	45	50	55
Grain Size (mm)	26.8 ± 23.3	37.1 ± 30.5	33.6 ± 25.5	11.6 ± 9.2	6.2 ± 4.7
Lamellar Spacing (nm)	920 ± 670	780 ± 560	660 ± 450	550 ± 390	470 ± 320
Yield Stress (MPa)	439 ± 11	458 ± 9	463 ± 7	471 ± 11	467 ± 13
Elongation (percent)	1.46 ± 0.21	1.47 ± 0.18	1.56 ± 0.15	1.52 ± 0.19	1.46 ± 0.20
Fracture Toughness (MPa m$^{1/2}$)	18.6 ± 2.6	20.4 ± 1.7	19.3 ± 2.2	21.0 ± 2.4	21.6 ± 3.1

Fig. 6—Microstructural characteristics of the CCDS specimens: (a) grain size, (b) lamellar orientation, and (c) lamellar spacing.
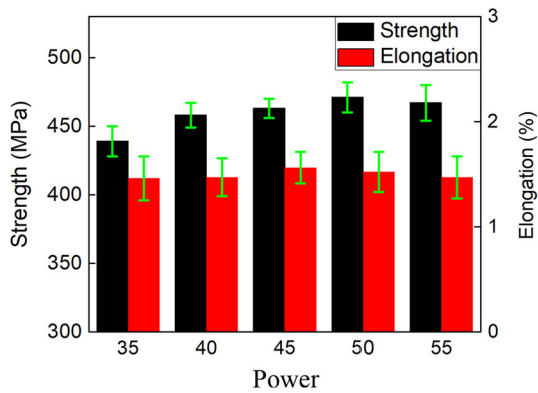
Fig. 7—Room-temperature tensile properties of the CCDS specimens at different power levels.
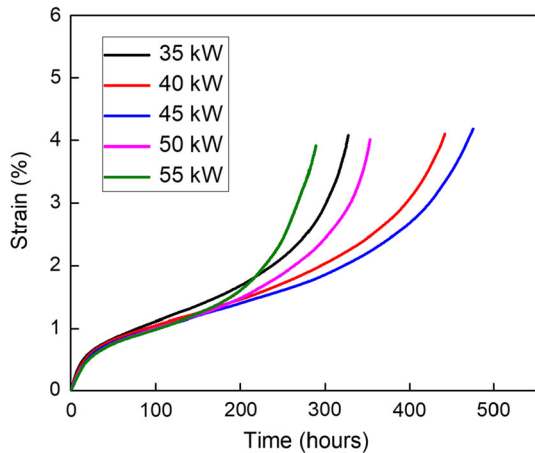

Fig. 8—Creep curves of the CCDS specimens at the power range of 35 to 55 kW performed under 830 °C/200 MPa.

tensile properties with yield strengths of 458 to 471 MPa and elongations of 1.46 to 1.56 pct.

The creep curves of the CCDS specimens at the power range of 35 to 55 kW performed in air at a testing temperature of 830 °C under a constant stress of 200 MPa are shown in Figure 8. All creep specimens were deformed until rupture. This alloy exhibits a longer creep life at a power of 40 and 45 kW and exhibits the shortest creep life at a power of 55 kW. All CCDS specimens exhibit a short steady-state creep stage, and then they transition to the acceleration creep stage. Previous studies revealed that the fine lamellar spacing could improve the creep properties.[28,29] However, in the current study, the CCDS specimen with the smallest lamellar spacing exhibits the shortest creep life, indicating that the creep life is affected not only by the lamellar spacing but also by the grain size, as described herebelow.

E. Crack Propagation During Creep

The γ-TiAl alloys usually have a short steady-state creep stage followed by a gradual tertiary creep leading to fracture at high temperatures or high stress.[19–21,28–33]

Therefore, the acceleration creep stage plays an important role in crack propagation. The nucleation/growth of the cavity and cracks usually occurs during the acceleration creep stage,[10] and it is essential to study the crack propagation behavior during creep. Figure 9 shows the microstructure of the CCDS alloy after the creep test at 830 °C under a constant stress of 200 MPa. Figures 9(a) and (b) correspond to Figure 2(c) prepared at 45 kW, while Figures 9(c) and (d) correspond to Figure 2(e) prepared at 55 kW. Figure 9(a) shows that typical cavities are located at the colony boundaries. The lamellar colony with the lamellar orientation parallel or perpendicular to the stress axis is regarded as being in a 'hard' orientation, and the lamellar colony with a lamellar orientation between 30 and 70 deg relative to the stress axis is regarded as being in a 'soft' orientation.[11,31] The angle between the lamellar orientation in the upper lamellar colony and the stress axis is 37.2 deg, and the angle between the lamellar orientation in the lower lamellar colony and stress axis is 9.2 deg. The plastic incompatibility between the hard and the soft lamellar colonies induces the formation of cavities at the colony boundary, after which the cavities grow and coalesce during creep.

An interlamellar crack is shown in Figure 9(b), as indicated by the white arrow. Only a small number of interlamellar cracks are observed in the lamellar structures. In addition, the main cracks are found at the colony boundary, as indicated by the black arrow. The microstructure in Figure 9(c) shows that the microcracks propagated along the intercolony boundary, and the lamellar orientations are marked with red lines. The crack tends to propagate along the colony boundary, as shown in regions A, B and C, with deflection being induced where the lamellae run perpendicular to the crack path. A smaller crack near the main crack is shown in Figure 9(d). The grain boundary is torn open along the direction of the shear stress during creep. The interlamellar cleavage fracture usually occurs during room-temperature tensile testing and is a typical characteristic of brittle fractures.

Previous studies have shown that the high Nb-containing TiAl alloys exhibited interlamellar cleavage fracture and small creep strain during creep below the brittle–ductile transition (BDT) temperature and exhibited intergranular fracture (ductile fracture) and large creep strain during creep above the BDT temperature.[30] The BDT temperature of the fully lamellar TiAl alloy was previously determined to be 780 °C to 800 °C.[30,31] In the current study, the creep temperature of 830 °C is higher than the BDT temperature in previous studies. Moreover, CCDS alloys have a large creep strain and intergranular fracture characteristic, which indicates that the creep tests were performed above the BDT temperature. Therefore, the CCDS alloys display ductile fracture characteristics, and some interlamellar cracks were found in the matrix after the creep tests.

The tendencies for variation of the creep life and steady-state (minimum) creep rate are shown in Figure 10. The steady-state creep rate significantly decreases as the input power increases. In the current study, the alloys exhibit similar lamellar orientations in
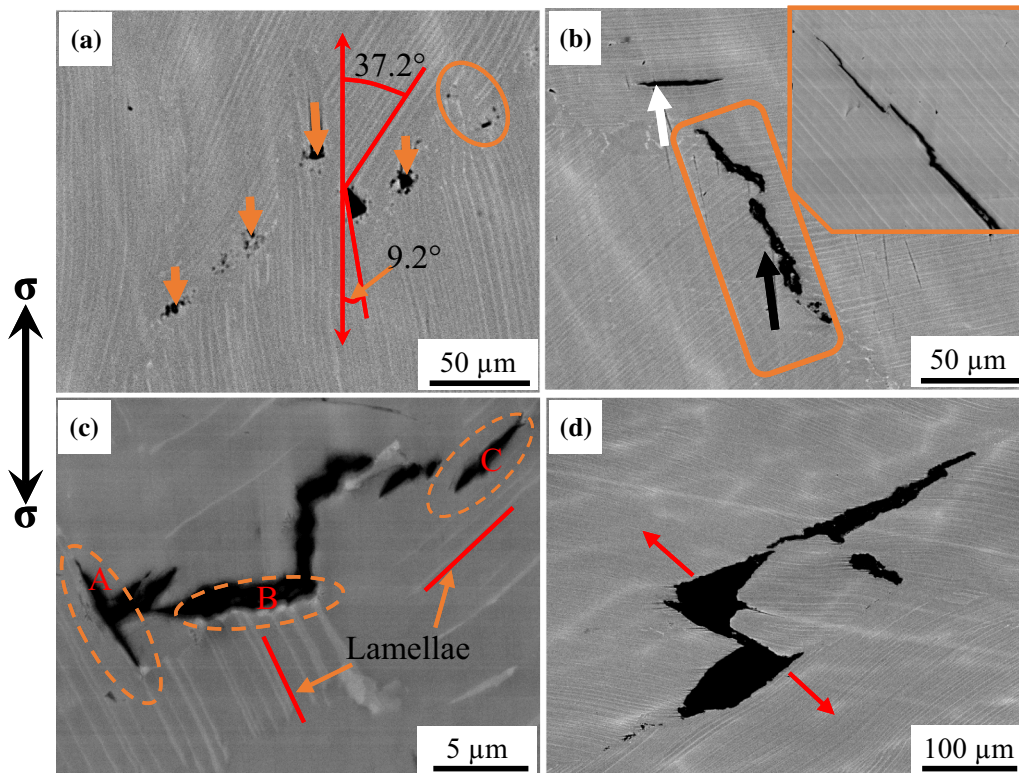
Fig. 9—Microstructure of the CCDS alloy after creep testing at 830 °C under a constant stress of 200 MPa. (*a*) and (*b*) alloys prepared at 45 kW; (*c*) and (*d*) alloys prepared at 55 kW. (a) The cavities at the colony boundary, (b) the interlamellar cracks and cracks at the colony boundary, (c) the magnified microstructure of a crack, and (d) cracks near the creep fracture location.
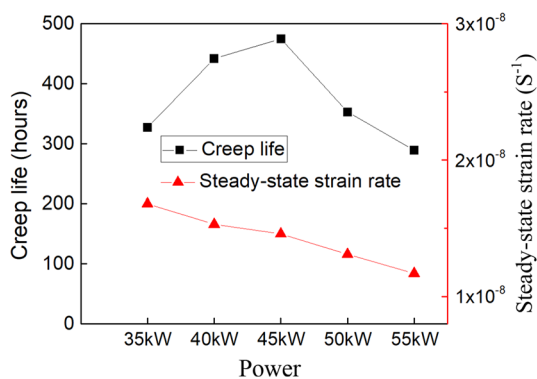

Fig. 10—Creep life and steady-state strain rate as a function of the growth rate at different power levels from 35 to 55 kW.

the input power range of 35 to 55 kW, indicating that the lamellar orientation has little influence on the creep rate. Maruyama *et al.*[19] reported that the creep rate is independent of the grain size (d) when $d > 100$ μm since the dynamic recrystallization at the colony boundary can increase the creep rate when $d < 100$ μm. Therefore, the steady-state creep rate is independent of the grain size in the current study. The steady-state creep rate decreases as the input power increases since the lamellar spacing decreases as the input power increases. The finer lamellar spacing reduces the effective slip length for dislocations and twins.[28] In the fully lamellar TiAl alloy, the low minimum creep

rate results in a long creep life. In the current study, the creep life of the CCDS is prolonged due to a well-developed DS microstructure.

The γ-TiAl alloys usually have a short steady-state creep, followed by a gradual tertiary creep leading to fracture at high temperatures or stresses. Thus, the tertiary creep has generally accounted for the majority of creep life in previous studies.[19–21,28–33] Similar results are observed in the current study, where the CCDS alloys exhibit a short steady-state creep, followed by a gradual tertiary creep that mainly affects the creep life. Moreover, in the fully lamellar TiAl alloy, the cavities and cracks usually nucleate and propagate at the colony boundaries due to the stress concentrations at these locations,[19,32] and the nucleation usually occurs during the acceleration creep stage (tertiary creep). The well-developed DS alloys mainly consist of vertical columnar crystals that can reduce the stress concentration at the colony boundaries. As a result, the nucleation rate of the crack/cavity at the colony boundary is reduced. Therefore, in the current study, the well-developed DS alloys (prepared at 40 and 45 kW) with the high steady-state strain rates exhibit the longest creep life. The formation of cracks/cavities in the matrix can release the local stress concentration during creep. The local stress concentration in the matrix is difficult to release in the well-developed DS alloys due to the low nucleation rate of cracks/cavities in the matrix; this induces the formation of interlamellar cracks in the well-developed DS alloy.
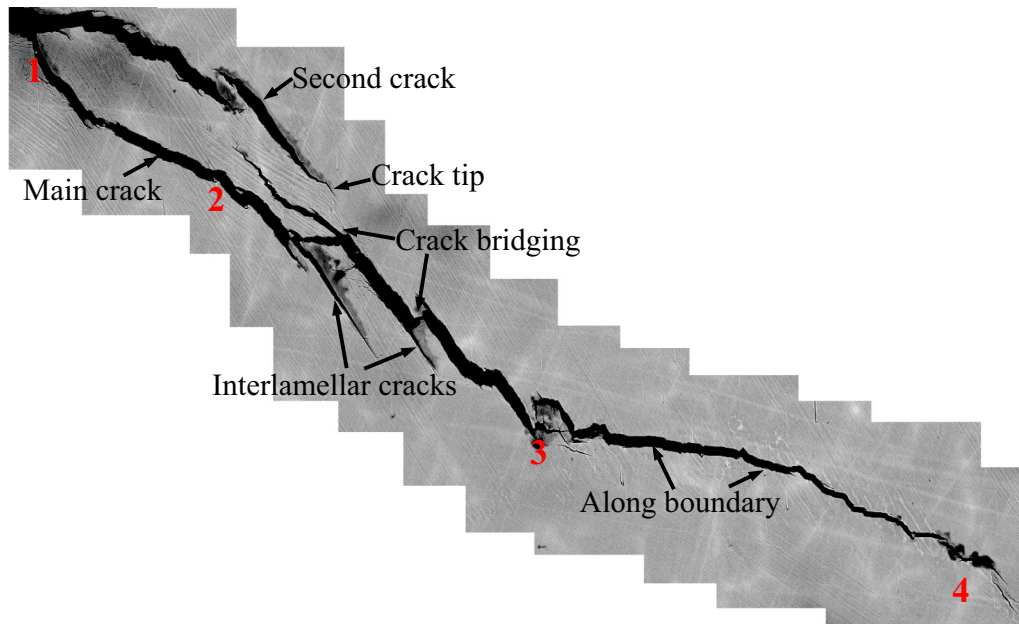
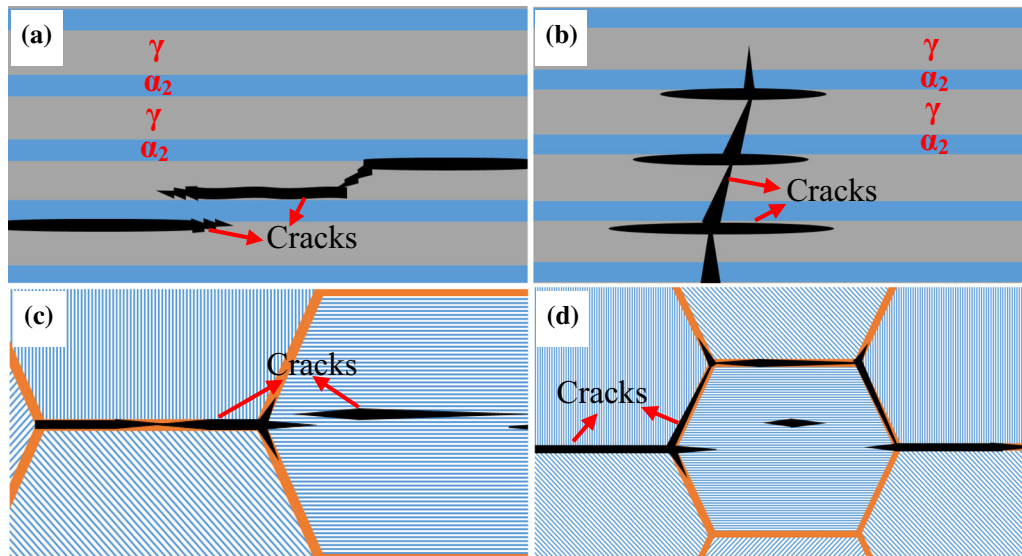Fig. 11—Corresponding crack propagation in the CCDS alloy prepared at 45 kW.

Fig. 12—Schematic illustration of crack propagation: (*a*) through (*c*) the crack propagation after fracture toughness testing, and (*d*) the crack propagation after creep testing.

F. *Fracture Toughness*

The average values of K_{IC} for the CCDS alloys in the input power range of 35 to 55 kW after the fracture toughness testing are shown in Table I. Figure 11 shows the crack propagation after the fracture testing in the CCDS specimen prepared at 45 kW. A translamellar crack is observed from point 1 to point 2, and a zigzag-like interlamellar crack is observed from points 2 to 3, while crack bridging is found at the adjacent interlamellar cracks. The crack propagation along the colony boundary is found from points 3 to 4. This result indicates that the crack is inclined to propagate along the colony boundary and lamellar interface after the crack intersects with them. The main reason for this phenomenon is that more energy is needed when the crack path crosses the α_2 lamellae.

To understand the fracture behavior in the current study, a schematic illustration of the crack propagation after the fracture toughness testing and creep testing is displayed in Figure 12. Figures 12(a) through (c) show the fracture behavior after the fracture toughness testing, revealing an interlamellar crack, translamellar crack, and intercolony boundary crack. Figure 12(d) shows the fracture behavior after the creep testing. The

main cracks are located at the colony boundary, and a few cracks are found at the lamellar interface because several cavities and cracks nucleate at the colony boundaries during creep. It is obvious that the well-developed DS alloy can significantly improve the creep properties because it reduces the nucleation rate of the crack/cavity at the colony boundary and delays intergranular fracture during tertiary creep. However, the well-developed DS alloy has little influence on the room-temperature tensile properties due to the cleavage fracture of the TiAl alloy during room-temperature tensile tests.

IV. CONCLUSIONS

1. The Ti-47Al-6Nb-0.1C alloy was prepared using the CCDS technique with input power ranging from 35 to 55 kW under a withdrawing velocity of 0.4 mm/min. These alloys exhibited typical β-solidification characteristics for an input power range from 40 to 55 kW. The well-developed DS microstructure was acquired at the input power of 40 and 45 kW.
2. With the increasing input power, the dendrite morphologies at the front of the L/S interface change from equiaxed grains to columnar grains and from columnar grains to equiaxed grains, and these changes depend on the temperature gradient and nucleation rate.
3. The lamellar spacing decreases with the increasing input power. The average room-temperature yield strength shows a tendency to increase with the increasing input power, and this tendency results from the decrease in the lamellar spacing.
4. The steady-state creep rate strongly depends on the lamellar spacing, and the creep life is affected by the DS microstructure. The well-developed DS alloy can significantly improve the creep properties but has little influence on the room-temperature tensile properties.
5. After fracture toughness testing at room temperature, the crack propagation shows an interlamellar crack, translamellar crack, and intercolony boundary crack. The cracks primarily propagate along the colony boundary after creep testing.

REFERENCES

1. G. Chen, Y. Peng, G. Zheng, Z. Qi, M. Wang, H. Yu, C. Dong, and G.T. Liu: *Nat. Mater.*, 2016, vol. 15, p. 876.
2. J.R. Yang, X.Y. Wang, B. Cao, Y.L. Wu, K.R. Zhang, and R. Hu: *Metall. Mater. Trans. A*, 2017, vol. 48, pp. 1–11.
3. J. Yang, X. Wang, B. Cao, Y. Wu, K. Zhang, R. Hu, and H. Fu: *Metall. Trans. A*, 2017, vol. 48, pp. 5095–5105.
4. G.L. Chen, X.J. Xu, Z.K. Teng, Y.L. Wang, and J.P. Lin: *Intermetallics*, 2014, vol. 15, pp. 625–31.
5. G. Yang, H.C. Kou, J.R. Yang, J.S. Li, and H.Z. Fu: *Acta Mater.*, 2016, vol. 112, pp. 121–31.
6. J. Li, Y. Liu, B. Liu, Y. Wang, P. Cao, C. Zhou, C. Xiang, and Y. He: *Intermetallics*, 2014, vol. 52, pp. 49–56.
7. H.Z. Niu, Y.Y. Chen, S.L. Xiao, and L.J. Xu: *Intermetallics*, 2012, vol. 31, pp. 225–31.
8. Q. Wang, R.R. Chen, Y.H. Yang, J.J. Guo, Y.Q. Su, H.S. Ding, H.Z. Fu, Adv. Eng. Mater., 2017, 1700734.
9. Z.C. Liu, J.P. Lin, S.J. Li, and G.L. Chen: *Intermetallics*, 2002, vol. 10, pp. 653–59.
10. HF Appel, JDH Paul, and M Oehring: *Gamma titanium aluminide alloys: science and technology*, Wiley-VCH, Weinheim, 2011 .
11. M. Yamaguchi, and H. Inui: In Structural Intermetallics, R. Darolia, J.J. Lewandowski, C.T. Liu, P.L. Martin, D.B. Miracle, and M.V. Nathal, eds., TMS, Warrendale, PA, 1993, pp. 127–42.
12. H. Inui, M.H. Oh, A. Nakamura, and M. Yamaguchi: *Acta Metall. Mater.*, 1992, vol. 40, pp. 3095–3104.
13. M. Yamaguchi, H. Inui, and K. Ito: *Acta Mater.*, 2000, vol. 48, pp. 307–22.
14. I.S. Jung, H.S. Jang, M.H. Oh, J.H. Lee, and D.M. Wee: *Mater. Sci. Eng. A*, 2002, vols. 329–331, pp. 13–18.
15. D.R. Johnson, H. Inui, S. Muto, Y. Omiya, and T. Yamanaka: *Acta Mater.*, 2006, vol. 54, pp. 1077–85.
16. J. Lapin and Z. Gabalcová: *Intermetallics*, 2011, vol. 19, pp. 797–804.
17. R.R. Chen, S.L. Dong, J.J. Guo, H.S. Ding, Y.Q. Su, and H.Z. Fu: *Mater. Des.*, 2016, vol. 89, pp. 492–506.
18. H.S. Ding, G. Nie, R.R. Chen, J.J. Guo, and H.Z. Fu: *Intermetallics*, 2012, vol. 31, pp. 264–73.
19. K. Maruyama, R. Yamamoto, H. Nakakuki, N. Fujitsuna, Mater. Sci. Eng. A, 1997, vol. s239–240, pp. 419–28.
20. D.I. Kimm and J. Wolfenstine: *Scr. Metall. Mater.*, 1994, vol. 30, pp. 615–19.
21. K. Xia, X. Wu, and J. Zhang: *Intermetallics*, 2003, vol. 11, pp. 325–30.
22. G. Nie, H.S. Ding, R.R. Chen, J.J. Guo, and H.Z. Fu: *Mater. Des.*, 2012, vol. 39, pp. 350–57.
23. J.D. Hunt and S.Z. Lu: Metall*Mater. Trans.*, 1996, vol. 27, pp. 611–23.
24. Q. Wang, H. Ding, H. Zhang, S. Liu, R. Chen, J. Guo, and H. Fu: *Mater. Des.*, 2016, vol. 99, pp. 10–20.
25. M.C. Flemings: *Metall. Trans. A*, 1991, vol. 22, pp. 957–81.
26. Z. Fan: *Int. Mater. Rev.*, 2002, vol. 47, pp. 49–85.
27. S. Muto, T. Yamanaka, H.N. Lee, D.R. Johnson, H. Inui, and M. Adv: *Eng. Mater.*, 2001, vol. 3, pp. 391–94.
28. Q. Wang, R.R. Chen, Y.H. Yang, S.P. Wu, J.J. Guo, Y.Q. Su, H.S. Ding, Y.Q. Su, and H.Z. Fu: *Mater. Sci. Eng. A*, 2018, vol. 711, pp. 508–14.
29. H. Zhu, D.Y. Seo, and K. Maruyama: *Scr. Mater.*, 2006, vol. 54, pp. 1979–84.
30. R.R. Chen, Q. Wang, Y.H. Yang, J.J. Guo, Y.Q. Su, H.S. Ding, and H.Z. Fu: *Intermetallics*, 2018, vol. 93, pp. 47–54.
31. Y.W. Kim and S.L. Kim: *Intermetallics*, 2014, vol. 55, pp. 92–101.
32. X.W. Du, J. Zhu, and Y.W. Kim: *Intermetallics*, 2001, vol. 9, pp. 137–46.
33. K. Xia, X. Wu, and D. Song: *Acta Mater.*, 2004, vol. 54, pp. 841–49.